Pulsed airborne lidar measurements of atmospheric optical depth using the Oxygen A-band at 765 nm

Haris Riris,[1,*] Michael Rodriguez,[2] Graham R. Allan,[2] William Hasselbrack,[2] Jianping Mao,[3] Mark Stephen,[1] and James Abshire[1]

[1]NASA Goddard Space Flight Center, 8800 Greenbelt Rd, Greenbelt, Maryland 20771, USA

[2]Sigma Space Corporation, 4600 Forbes Blvd., Lanham, Maryland 20706, USA

[3]Earth System Science Interdisciplinary Center (ESSIC), University of Maryland, College Park, Maryland 20740, USA

*Corresponding author: Haris.Riris@nasa.gov

Received 26 April 2013; revised 22 July 2013; accepted 24 July 2013;
posted 31 July 2013 (Doc. ID 189527); published 30 August 2013

We report on an airborne demonstration of atmospheric oxygen optical depth measurements with an IPDA lidar using a fiber-based laser system and a photon counting detector. Accurate knowledge of atmospheric temperature and pressure is required for NASA's Active Sensing of CO_2 Emissions over Nights, Days, and Seasons (ASCENDS) space mission, and climate modeling studies. The lidar uses a doubled erbium-doped fiber amplifier and single photon-counting detector to measure oxygen absorption at 765 nm. Our results show good agreement between the experimentally derived differential optical depth measurements with the theoretical predictions for aircraft altitudes from 3 to 13 km.

OCIS codes: (010.0280) Remote sensing and sensors; (280.1910) DIAL, differential absorption lidar; (280.3640) Lidar; (300.1030) Absorption.

http://dx.doi.org/10.1364/AO.52.006369

1. Introduction

Accurate measurements of greenhouse gas mixing ratios on a global scale are needed to gain a better understanding of climate change and its possible impact on our planet. Atmospheric carbon dioxide (CO_2) is currently recognized as having the largest radiative forcing of all greenhouse gases [1]. The current volume mixing ratio of CO_2 is 390 ppm (parts per million), a significant increase since the preindustrial age level of ~280 ppm. The widespread use of fossil fuels and other anthropogenic sources has been blamed for a large part of the increase but there is still uncertainty on the future impact of CO_2 on climate change. CO_2 has both natural and anthropogenic sources and sinks, some of which are not very well understood or accurately measured on a global scale. In order to reduce the uncertainty in the carbon budget, the last US National Research Council (NRC) Decadal Survey for Earth Science [2] has recommended that NASA implement a laser-based space mission, Active Sensing of CO_2 Emissions over Nights, Days, and Seasons (ASCENDS), to measure CO_2 emissions.

The ASCENDS mission is planned to have sufficient accuracy (1–2 ppm) to infer regional CO_2 terrestrial and oceanic sources and sinks. The science objectives for ASCENDS [3] are to (1) quantify global spatial distributions of atmospheric CO_2 on scales of weather models in the 2010–2020 era; (2) quantify the current global spatial distribution of terrestrial and oceanic sources and sinks of CO_2 on $1° \times 1°$ grids at weekly resolution; and (3) provide a scientific basis for future projections of CO_2 sources and sinks through data-driven enhancements of Earth system process modeling. The ASCENDS working group is currently in the process of determining the

1559-128X/13/256369-14$15.00/0

requirements for the mission in order to meet its science goals [3]. The requirements will affect the instrument design and the overall mission architecture. Our approach, which uses integrated path different absorption (IPDA) lidar, has been designed to limit the many potential random and systematic error sources.

A. Need for Pressure Measurements

The goal of ASCENDS is to derive the atmospheric CO_2 mole fraction in parts per million volume (ppmv), $X(CO_2)$, relative to dry air:

$$X(CO_2) = \frac{N(CO_2)}{(1 - X(H_2O))N(\text{Air})}, \quad (1)$$

where $N(CO_2))$ is the CO_2 number density measured by a laser-based sensor, $X(H_2O))$ is the water vapor mixing ratio, and $N(\text{Air})$ is the air number density, or the number density of the air molecules. $N(CO_2)$, $X(H_2O)$, and $N(\text{Air})$ are all needed to derive $X(CO_2)$. In North America and most of Eurasia, pressure measurements can be obtained by local weather stations and other meteorological sensors. However, the global coverage of these sensors is not sufficient to meet the ASCENDS requirements in sparsely populated areas such as sub-Saharan Africa and the South Pacific. Since oxygen (O_2) is a stable and uniformly mixed molecule in the atmosphere at 20.95%, the measurement of oxygen absorption can be used to infer the dry air density of CO_2 provided the water vapor mixing ratio is known or can be obtained by additional observations. The impact of pressure measurements and other meteorological parameters on the accuracy and precision requirements for ASCENDS is currently an active topic of discussion and is the object of several observing system simulation experiments. The current recommendation from the ASCENDS working group is that "co-located surface pressure measurements" are needed for ASCENDS and that "the currently available surface pressure forecasts and/or re-analyses from numerical weather models [are] insufficiently accurate, especially over sparsely observed areas, to relax the need for concurrent measurement of pressure" [3]. Although no formal pressure measurement requirement has been released yet, we anticipate that an error of ~0.2% will be needed in order to keep the $X(CO_2)$ error below 1 ppm.

Lidar measurements using oxygen absorption to infer pressure have been previously demonstrated [4–7] but the lidar performance was hampered by limited laser and detector technology available at the time. Today with the availability of fiber amplifier technology, and sensitive photon-counting detectors, the technique is feasible from airborne and spaceborne platforms. Our approach uses integrated differential path absorption (IDPA) with a sequence of laser pulses at increasing wavelengths that sample a pair of absorption lines in the Oxygen A-band at 764.7 nm. The O_2 lines were selected after careful spectroscopic analysis to minimize the O_2 line temperature dependence and the availability of the transmitter and receiver technology to maximize transmitter power, doubling efficiency, and detector sensitivity [8]. Although in principle only two wavelengths "on" and "off" the line are needed to determine the transmittance through the atmospheric column, in practice, several wavelengths should be used to sample the lines. Using multiple wavelengths can adequately sample instrumental and systematic errors, such as etalon fringes and baseline structure, that may be undersampled with the two-wavelength approach. It may also allow the retrieval of additional spectroscopic parameters such as pressure shift. Some of the trades and signal to noise comparisons of different IPDA approaches have been discussed by Sun and Abshire [9]. In general, if the only noise source in the system is random noise (e.g., shot noise) that is uniformly distributed across the absorption lineshape, using multiple wavelengths to sample the absorption would not provide any improvement. However, in any realistic laser spectrometer, systematic "noise" sources or drifts are not evenly distributed across all wavelengths and will limit the accuracy and precision by a few orders of magnitude above the shot noise limit [10]. This "noise" typically forms a time-varying background structure that is superimposed on the signal that needs to be adequately sampled and, if possible, modeled and filtered. Depending on the spectral distribution and time dynamics of the systematic background structure, it may be impossible to adequately sample it by using only two wavelengths. Furthermore, the signal-to-noise ratio (SNR), which is typically the signal divided by the variance of the total, normally distributed noise, may not adequately describe the performance of a system with pink noise or drifts. Werle discusses in detail the concept of Allan variance, which is a better metric to use, in systems where the variance may remain the same but the mean varies over time [10].

Figure 1 shows the O_2 absorption lines we selected and our current choice of wavelengths across the lines. The 2008 HITRAN database [11] and a US standard atmosphere were used for the transmittance calculation.

The O_2 lidar is a nadir pointing instrument that measures the total transmittance, $\tau(\nu)$, of the emitted laser energy E_o, through the atmospheric column. The received energy E, at each wavelength, is proportional to the receiver photon-counting efficiency η, the ground surface reflectivity ρ, and the collecting area of the receiver A, and is inversely proportional to the square of the range to the surface R:

$$E = E_0 \eta \frac{A}{R^2} \frac{\rho}{\pi} \tau^2(\nu). \quad (2)$$

If the attenuation due to scattering is ignored, the total transmittance at a single frequency (wavelength) over the atmospheric column is an integral

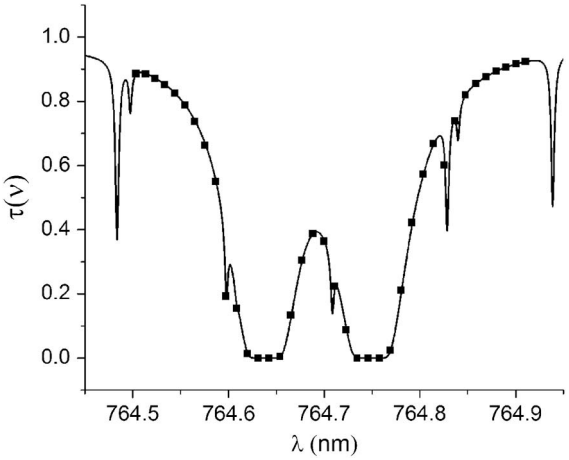

Fig. 1. Atmospheric transmittance from a 13 km altitude showing the Oxygen A-band absorption line at 764.7 nm using a standard US Atmosphere, the HITRAN 2008 database (solid line), and our choice of wavelengths (solid squares). The smaller absorptions are O_2 isotope lines.

over all vertical atmospheric layers, dr, between the aircraft and the ground:

$$\tau(\nu) = e^{-2\int_0^R \sigma(\nu)N(r)\mathrm{d}r}, \tag{3}$$

where $\sigma(\nu)$ is the molecular absorption cross section for a given atmospheric layer and $N(r)$ is the O_2 number density in each atmospheric layer. Substituting $\tau(\nu)$ into Eq. (2), we get

$$E = E_0\eta\frac{A}{R^2}\frac{\rho}{\pi}e^{-2\int_0^R \sigma(\nu)N(R)\mathrm{d}r}. \tag{4}$$

For an IPDA lidar that uses only two wavelengths ("on" and "off" the absorption, λ_{on} and λ_{off}), Eq. (4) for the two wavelengths can be written as

$$\frac{E_{on}}{E_{off}} = \frac{E_{0on}}{E_{0off}}\eta\frac{A}{R^2}\frac{\rho}{\pi}e^{-2\int_0^R (\sigma(\nu)_{on}-\sigma(\nu)_{off})N(r)\mathrm{d}r}. \tag{5}$$

The differential optical depth (DOD) for the "on" and "off" wavelengths is defined as the natural logarithm of the transmitted and received energy ratios:

$$\mathrm{DOD} = \frac{1}{2}\ln\left[\frac{E_{off}}{E_{on}}\times\frac{E_{0on}}{E_{0off}}\right]. \tag{6}$$

The DOD value is, of course, dependent on the wavelengths chosen as the "on" and "off" wavelengths. Typically the "on" wavelength (λ_{on}) is chosen to be at the peak of the absorption line and the "off" (λ_{off}) wavelength is chosen to be at the wing of the absorption feature of interest. The SNR for an IPDA lidar is dependent on the selection of the on and off wavelengths and the corresponding $\mathrm{SNR_{ON}}$ and $\mathrm{SNR_{OFF}}$. The random error in the O_2 column number density is then given by

$$\varepsilon = \frac{-1}{\ln\left(e^{-2\int_0^R (\sigma(\nu)_{on}-\sigma(\nu)_{off})N(r)\mathrm{d}r}\right)}\times\left(\frac{1}{\mathrm{SNR_{OFF}}}+\frac{1}{\mathrm{SNR_{ON}}}\right). \tag{7}$$

For detailed sensitivity and various SNR analyses for an IPDA, see [12–18]. For the O_2 lines we selected, the peak of the absorption is optically thick [i.e., the optical depth (OD) is greater than 100] so it is not suitable to use as an "on" wavelength since there virtually is no signal. Instead, the trough between the two absorption lines at 764.684 nm, which is not optically thick and is sensitive to pressure changes, is used as the "on" wavelength. For the "off" wavelength, we use the average OD value at the beginning and the end of our scan (764.5 and 764.9 nm, respectively).

To first-order, the DOD depends linearly on small changes in pressure and range [15]. The DOD can be used to assess the performance of an IPDA lidar independent of other ancillary parameters, such as atmospheric column temperature. Figure 2 shows the expected OD lineshapes and the corresponding OD values at λ_{on} and λ_{off} along with $\mathrm{DOD} = \mathrm{OD}(\lambda_{on}) - \mathrm{OD}(\lambda_{off})$ as a function of pressure for a 13 km horizontal path and as a function of altitude for a standard US Atmosphere. A Voigt profile [19,20] and the 2008 HITRAN database were used for these calculations. Recent spectroscopic studies, however, suggest that more complex profiles that include Dicke narrowing [21] and line mixing should be considered [22–24].

For an IPDA lidar that uses multiple wavelengths, Eq. (4) can be modified to account for all the discrete wavelengths used:

$$E_j = E_{0j}\eta_j\frac{A}{R^2}\frac{\rho_j}{\pi}e^{-2\int_0^R \sigma(\nu_j)N(R)\mathrm{d}r}, \tag{8}$$

where j is the wavelength index. For our IDPA lidar, the entire experimentally derived lineshape over all wavelengths is fitted to a theoretical calculation of the expected transmittance by minimizing the root mean square difference ε between them,

$$\varepsilon = \sqrt{\left[\sum_{j=1}^{M}[\tau^{\mathrm{theory}}(\nu_j) - \tau^{\mathrm{experiment}}(\nu_j)]^2/M\right]}, \tag{9}$$

where M is the total number of wavelengths used. The multiwavelength fitting process should reduce the effects of some systematic errors, such as etalon fringes and baseline drifts, since it samples the lineshape instead of just two "on" and "off" points.

2. Airborne Instrument Description

Our present instrument (Fig. 3) uses a continuous wave distributed feedback (DFB) diode laser (FITEL FRL15DCWD-A61-19600-C), operating at 1529.4 nm, whose current and temperature are controlled by a

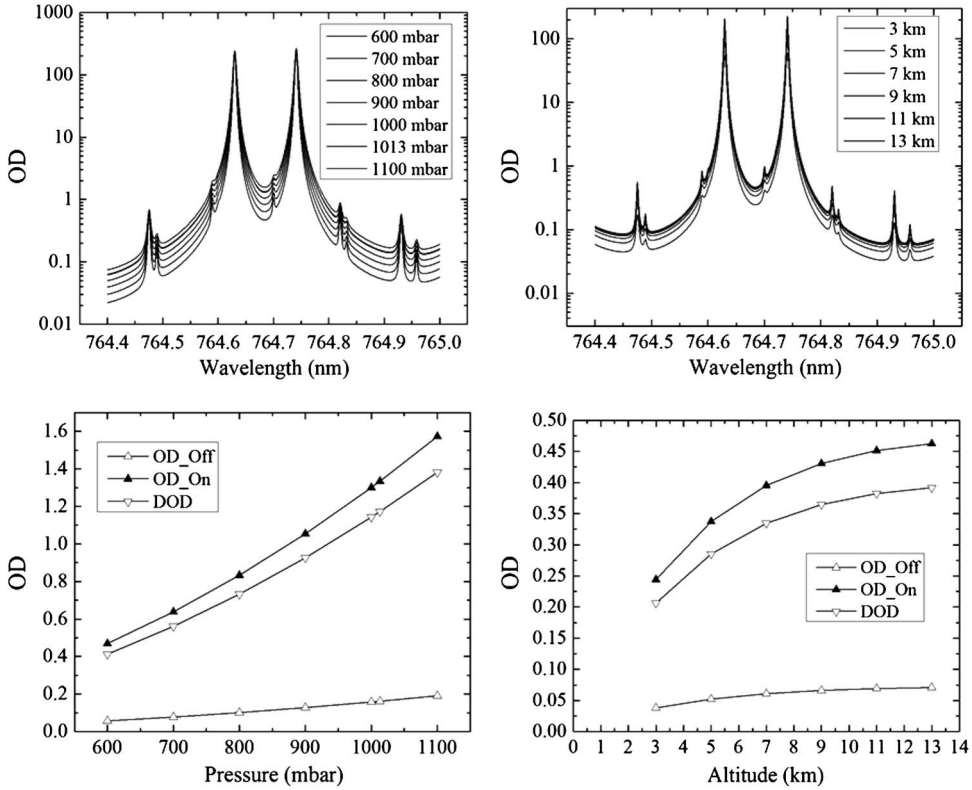

Fig. 2. Oxygen optical depth lineshapes as a function of pressure for a 13 km horizontal path (top left) and as a function of altitude for a standard US Atmosphere (top right) and the corresponding OD values at λ_{on} and λ_{off} and DOD = OD(λ_{on}) – OD(λ_{off}) as a function of pressure (bottom left) and the OD values at λ_{on} and λ_{off} and DOD as a function of altitude (bottom right).

commercial laser driver (EM4 part no: EM451). The diode laser wavelength is rapidly scanned (at 250 Hz) over the O_2 absorptions by applying a voltage ramp waveform to the drive current. The frequency, amplitude, and shape of the wavelength scan waveform are easily adjusted using a computer-controlled waveform generator. A wavelength calibration procedure using a heterodyne technique, a wave meter (Burleigh WA-1650), and a stabilized 1529 nm laser source provides an accurate calibration of our wavelength scan. The inherent diode laser linewidth is very narrow (~1 MHz depending on the laser driver used). The output of the diode laser is externally modulated (chopped) with a fiber-coupled acousto-optic modulator (AOM) to yield relatively short (~250 ns FWHM) laser pulses with approximately 30 dB extinction ratio. The pulse frequency and pulse shape and width are easily adjusted by modifying the analog waveform applied to the AOM (EM4 part no: EM417).

A master trigger, from a GPS receiver 1 pulse per second signal, initiates a wavelength scan with 40 laser pulses separated by 100 μs (~0.011 nm) that are used to sample the oxygen absorption lines (Fig. 4). The last two pulses in the scan occur during the ramp waveform flyback and are not used for data analysis. The 100 μs time separation between pulses (equivalent to a range of 15 km) ensures that all wavelengths are sufficiently separated in time and only one wavelength is detected by the receiver at a time. The optical pulses from the AOM are amplified by an erbium-doped fiber amplifier (EDFA) made by NP Photonics (custom item).

The EDFA output is directly fiber-coupled into a periodically poled KTP crystal (PPKTP) assembly (AdVR custom item), which frequency doubles the 1529.4 nm laser radiation to 764.7 nm. The free-space output from the doubling crystal is directed to the transmit optics assembly which includes two turning mirrors, a beam expander to reduce the

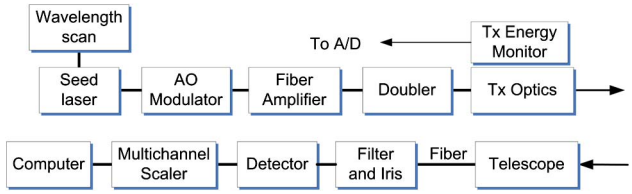

Fig. 3. Functional block diagram of the oxygen lidar as flown on the DC-8.

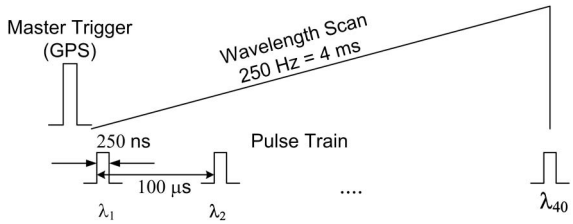

Fig. 4. Timing sequence of the oxygen lidar.

Table 1. Oxygen Lidar Parameters

Parameter	Value
Center ("on") wavelength	764.685 nm
"Off" wavelengths	764.5 and 764.9 nm
Pulse rate	10 kHz
Pulse width	250 ns
Energy/pulse	~2.0 μJ
Scan rate	250 Hz
Wavelength spacing	~0.011 nm
Histogram bin width	32 ns
Divergence	110 μrad
Receiver diameter	20 cm
Receiver field of view	200 μrad
Receiver bandpass	0.5 nm (FWHM)
Scan rate	250 Hz
Averaging period	1 s
Detector efficiency	~50%

beam divergence to 110 μrad and an integrating sphere with an energy monitor detector (Thorlabs PDA36A). The output signal from the energy monitor is integrated by a gated integrator (Signal Recovery Model 4121B) and then digitized by an analog-to-digital converter (ADC) to accurately measure the laser pulse energy. The transmitted laser pulses travel through the aircraft nadir port to the ground. The nadir port windows are antireflection (AR) coated for 765 nm and are wedged to minimize back reflections into the receiver and unwanted etalon fringes. The spot size from a 10 km altitude is 1.1 m and the separation between successive pulses (wavelengths) is 2 cm, using a nominal aircraft speed of 200 m/s. This separation minimizes the changes in reflectivity between successive wavelengths. The reflected ground echoes are collected by a commercial 20 cm diameter receiver telescope (Vixen VC200L) and are coupled into an AR-coated 400 μm core multimode fiber (Fiberguide CB18166). The receiver field of view (FOV) is determined by the telescope effective focal length (~2 m), the receiver fiber core size, and its numerical aperture (NA). In our case, the receiver FOV is 200 μrad. The fiber output from the receiver is collimated and directed through a narrow (0.5 nm FWHM) bandpass filter made by Barr Associates, an adjustable iris to adjust the amount of light onto the detector, and then focused onto a single photon-counting module (Perkin Elmer SPCM-AQRH-12). The fiber collimator, filter, iris, and focusing lens reside in a single optomechanical assembly to minimize alignment sensitivity and optimize the transmission of the bandpass filter. The SPCM output is sent to a multichannel scaler (Quantar technology P7889), which produces a histogram of the return pulses as a function of time (or range) over the entire atmospheric column. The bin width for the histogram was 32 ns. The computer then averages, digitizes, and stores the histograms over 1 s. The averaging period is adjustable but is limited by the data transfer rate. The duty cycle for the data acquisition was 90%. By digitizing the entire atmospheric column we can separate contributions from clouds and the ground, and determine the range, R, to the ground using the time of flight (TOF) of the first laser pulse [25]. The parameters of the airborne system are summarized in Table 1, and Fig. 5 shows a 1 s average histogram return from one of our flights over Wisconsin and an expanded view of a single pulse.

3. Airborne Campaign

We have demonstrated O_2 measurements using the multiwavelength IPDA technique from the ground and from NASA's DC-8 airborne laboratory-based in Palmdale, California. In 2010 and 2011, we participated in a multi-instrument airborne campaign sponsored by the NASA ASCENDS program to measure CO_2 and O_2 fluxes in the United States. The O_2 lidar was part of a Goddard Space Flight Center (GSFC) instrument which included a CO_2 lidar [11] and an *in situ* cavity ring down spectrometer (Picarro G1301-m). Five flights in the continental US (CONUS) were carried out in 2010, and seven science flights in CONUS and British Columbia, Canada in 2011. The O_2 lidar collected data for two of the 2010 and all seven of the 2011 flights. In this paper, we will present data from the 2011 flights.

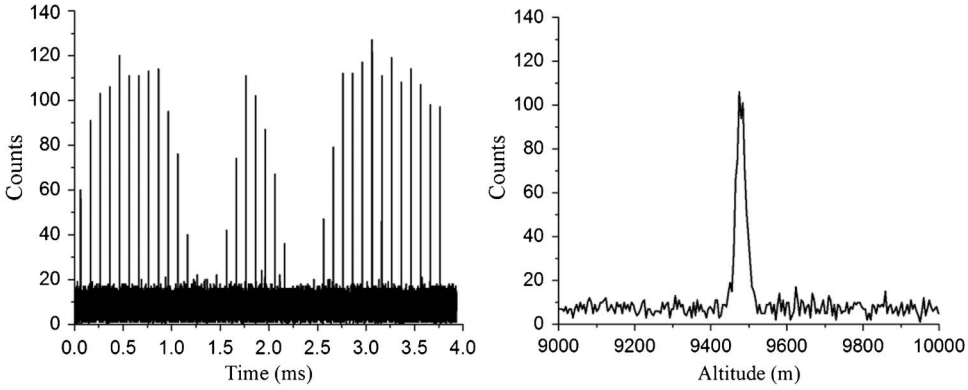

Fig. 5. Example of a histogram return as a function of time from an altitude of ~10 km during a flight over central Wisconsin (left) and an expanded view of a single-return pulse (right) as a function of altitude (range). The integration time was 1 s and the measurement time bin resolution was 32 ns.

Table 2. 2011 Science Flight Summary

Flight No/Color	Flight Date	General Location	Duration (Hours)
1/Red	7/28/2011	Central Valley, California	4.4
2/Orange	8/2/2011	Pacific Ocean, Baja, California	3.3
3/Magenta	8/3/2011	Railroad Valley, Nevada	4.6
4/Green	8/7/2011	Pacific Northwest, British Columbia	7.7
5/Purple	8/9/2011	Four Corners, New Mexico	5.5
6/Light Blue	8/10/2011	California to Iowa and Minnesota	6.5
7/Dark Blue	8/11/2011	Minnesota, Wisconsin to California	7.0

The 2011 flights typically included multiple segments at increasing altitudes from 3 to 13.5 km over varying topography and atmospheric conditions. In addition, for most flights, a spiral descent from ~13.5 km to near the surface (30–70 m) was included in the flight plan in order to sample vertical profiles of meteorological parameters (pressure, temperature, humidity, etc.) using the aircraft's data acquisition system and the CO_2 mixing ratio profile using the *in situ* sensor. For two flights (flight 1 over the Central Valley of California and flight 3 over Railroad Valley in Nevada), radiosonde balloons were also released near the spiral location and provided additional independent meteorological measurements and allowed us to estimate the vertical structure of the atmosphere at the same location and validate O_2 lidar measurements. Table 2 and Fig. 6 summarize our 2011 science flights and Fig. 7 shows the main flight path and altitude profile for flight 1 (in the Central Valley of California). All flights except the last two originated from and ended in the Dryden Airborne Operations Facility in Palmdale, California, where the NASA DC-8 aircraft is based. Flight 6 originated in Palmdale and landed in Minneapolis after overflying most of the western United States and Iowa, and flight 7 originated in Minneapolis and overflew a Total Carbon Column Observing Network site in Park Falls, Wisconsin (https://tccon-wiki.caltech.edu/Sites/Park_Falls) before returning to Palmdale.

A. Retrievals and Analysis

Our retrieval algorithm follows the approach of Rodgers [26] and is similar to the one outlined by Kawa *et al.* [27] and Abshire *et al.* [13] in their CO_2 simulations and airborne retrievals. The algorithm estimates the column average O_2 transmittance of the atmospheric column by integrating the pulse returns from the surface echo signals at each wavelength after normalizing by the transmitted pulse energy, the filter transmission, and other instrument calibrations. The algorithm then compares the experimental with the theoretically calculated transmittance values and adjusts the fit parameters

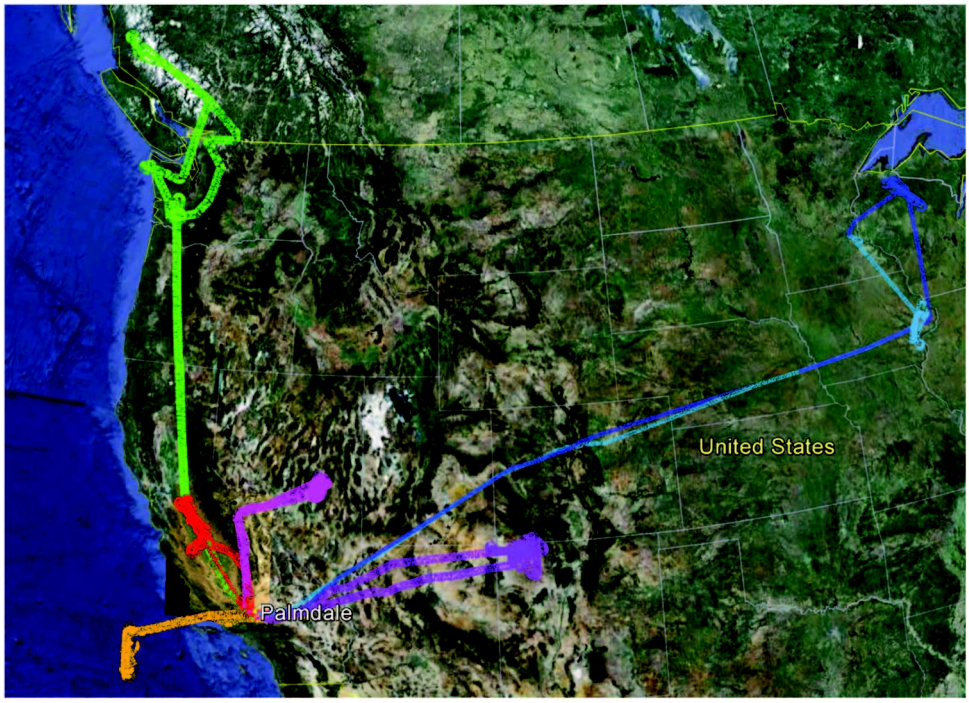

Fig. 6. Summary of 2011 science flights over varying topography, elevation, surface reflectivity, ground cover, and weather conditions. The colored trajectories identify each flight.

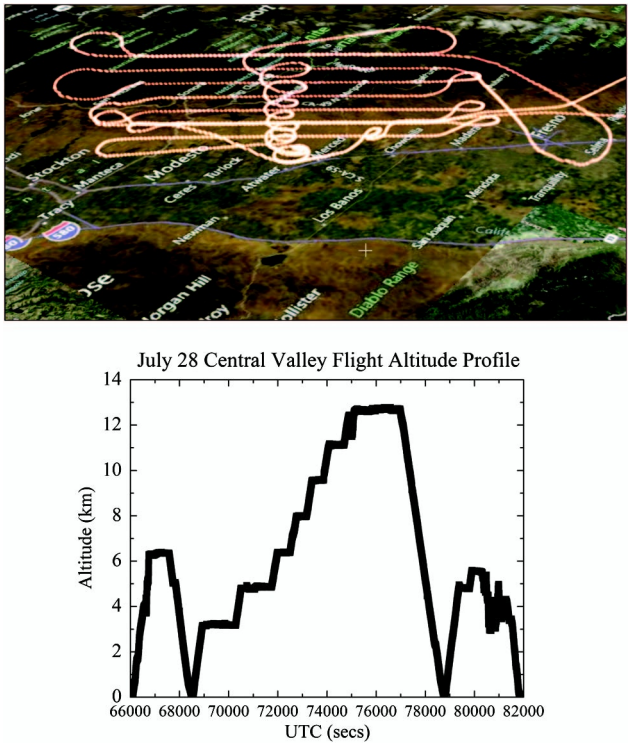

Fig. 7. Flight 1 on July 8, 2012, originated in Palmdale, California, and the constant altitude legs from 3 to 13 km traversed a north–south path from Fresno to Stockton in California's Central Valley. The spiral occurred at Castle Airport in Atwater, California.

to minimize the error. The theoretical calculations use a Voigt lineshape, the vertical profile of the atmosphere, the lineshape parameters from the HITRAN 2008 database [11], and line by line radiative transfer calculations [28]. The theoretical and experimental DOD values are determined by the difference in OD between the trough at 764.684 nm ("on" wavelength) and the average value of the OD at the start and end wavelengths of our scan at 764.5 and 764.9 nm, respectively, ("off wavelengths"). The experimental OD values are taken from the fit. The range (path length) from the aircraft to the surface is determined from the laser pulse TOF following the approach suggested by Amediek *et al.* [25] by correlating the first return pulse with the outgoing energy monitor pulse and measuring the time delay of the correlation peak. The meteorological data for the vertical profile of the atmosphere for most flights are obtained from the spiral descent or the Goddard Modeling and Assimilation Office (GMAO) [29].

The vertical profile of the atmosphere will, of course, change as a function of time, location, altitude, and topography. For short and localized flights, such as flights 1, 3, and 5, over a relatively flat topography and constant meteorological conditions, the spiral data are a fairly good representation of the state of the atmosphere for the entire flight. For long flights spanning a large area with varying topography, such as flights 4, 6, and 7, the spiral data (obtained over the coast of Washington state, western Iowa, and northern Wisconsin, respectively) are not a good representation of the vertical structure of the atmosphere for the entire flight. Additional meteorological data were obtained from GMAO modern era retrospective-analysis for research and applications (MERRA, http://gmao.gsfc.nasa.gov/research/merra/index.php) along the flight paths with a sampling/interpolating interval of 5 min and using the 42 lowest atmospheric levels.

Most of the flight locations for the 2011 airborne campaign were selected to test the performance of the CO_2 lidars at 1572 nm over surfaces of different reflectivity and topography, and were not necessarily optimized for testing the performance of the O_2 lidar measurements at 765 nm. Flights 1, 4, 5, 6, and 7 were used to analyze performance of the O_2 lidar. Flight 2 was mostly over a low, dense cloud cover and since it was over the Pacific Ocean, we lacked the *in situ* data that was needed to generate the atmospheric profiles. Flight 3 was carried out to test the CO_2 lidars over a very small area of constant reflectivity (railroad valley, Nevada) which is used as a calibration site for space-borne passive spectrometers (GOSAT and OCO-2 in the future). The valley is less than 50 km long and is surrounded by high peaks and complex topography on both sides. In addition, the constant altitude flight segments were very short (typically <5 min) and were not very useful in assessing the O_2 lidar performance.

Flight 1, on July 29, 2011, was a calibration flight over a fairly flat terrain and constant CO_2 mixing ratios. The flight spanned most of California's central valley in a north–south direction, roughly from Fresno to Stockton, and the spiral occurred at Castle Airport in Atwater, California, approximately in the middle of the constant altitude segments of the flight (see Fig. 7). The theoretical DOD predictions for flight 1 were calculated using the meteorological data from the spiral and GMAO.

The spiral data for this flight should be a good representation of the state of the atmosphere for the entire flight since the meteorological conditions did not change significantly in the central valley. Although we used 38 wavelengths to sample the absorption, we selected only 27 for the retrievals. The points with near zero transmittance (or very high OD values) can bias the error estimation and were not used in the fitting process. However, these points can be useful in determining the zero percent transmittance of the system and account for any instrumental systematic errors, such as electronic offsets. In addition, most of the points coincident with the weaker isotopic O_2 absorptions were not used. Figure 8 (left panel) shows an example of our experimental lineshape data and a sample fit to the theoretical transmittance from flight 1 from an altitude of 12.2 km. The change in DOD as a function of altitude and a comparison with the theoretical predictions for the entire flight 1 is also shown in Fig. 8 (right panel). The averaging period was 60 s. The experimental data agreed well with predictions for all flight altitudes from 3 to 13.5 km, and the

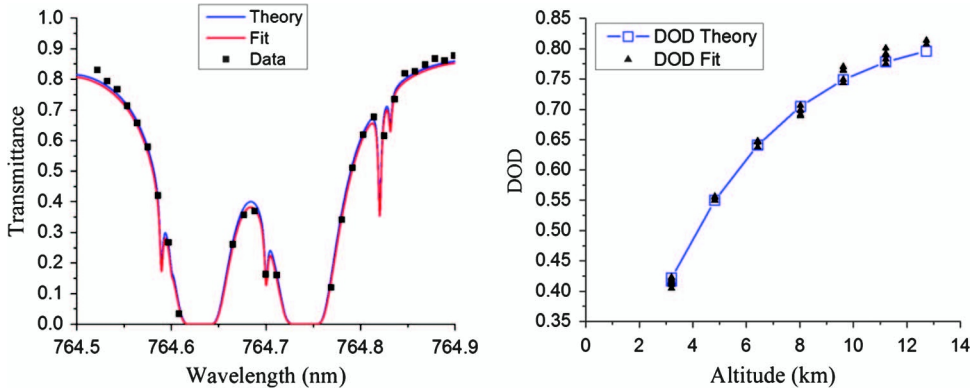

Fig. 8. (Left) An experimental OD line shape (solid squares) from flight 1 on July 28th, 2012, with the theoretical prediction (blue) and the best fit (red). The altitude was 12.2 km and the averaging period was 60 s. (Right) The change in DOD versus altitude agreed well with the theoretical predictions after a bias adjustment of 8%.

corresponding change in DOD agreed well with the predicted values after a constant scaling factor for all altitudes of approximately 8% was applied to the predicted values. Another way to visualize the DOD data is to plot the experimentally derived DOD versus the theoretically calculated values. Figure 9 shows a plot of the experimentally derived DOD versus the theoretically calculated DOD values along with a linear fit. The slope of the linear fit was 1.0037 ± 0.0028 and the intercept was -0.0021 ± 0.0016 and the R^2 value was 0.99987. Using flight 1 as a calibration, we applied the constant scaling factor of 8% to the predicted values of all the other flights.

Flight 4, over the Cascades mountain range in the Pacific Northwest and British Columbia, was intended to test the performance of the CO_2 lidar systems over snow (the reflectivity of snow is very low at 1572 nm, the CO_2 wavelength, but high at 765 nm, the O_2 wavelength). The segments over the Canadian Cascades in British Columbia proved to be problematic for the O_2 analysis due to the very steep and rapidly varying terrain; the intermittent snow cover, which stressed the dynamic range of the SPCM; and the very high background counts due to the high snow reflectivity. Thus, for the O_2 analysis, we used only the transit over California and Oregon. The experimental DOD versus theoretical DOD predictions for the California–Oregon segment of the flight are shown in Fig. 10 (left panel). A 10 s average was used. The theoretical DOD predictions were calculated using meteorological data from the GMAO interpolated every 1 s. The flight segment spanned over 1100 km and the meteorological data from the spiral, which occurred in Washington State, cannot be used for the entire flight. The agreement between theory and experiment for this segment of the flight was very good, as shown in Fig. 10 (left panel).

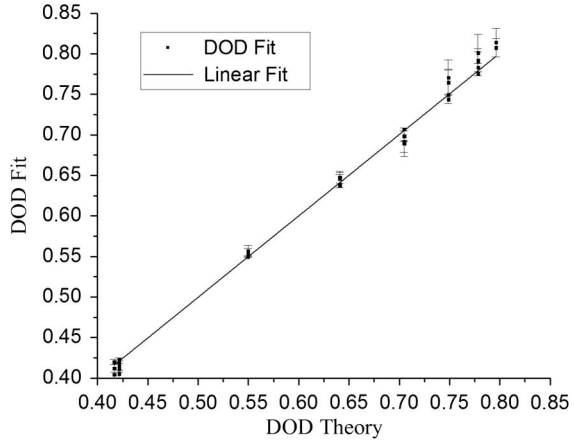

Fig. 9. Experimentally derived DOD versus the theoretically calculated DOD values. The slope of the linear fit was 1.0037 ± 0.0028 and the intercept was -0.0021 ± 0.0016.

Flight 5 was done mostly at constant, relatively low altitude (~4.5 km) over relatively flat terrain to measure CO_2 emissions from the Four Corners power plant in New Mexico. Although it was not well suited for O_2 (pressure) measurements, we analyzed the entire flight from Palmdale to the Four Corners power plant and back. Again, the theoretical DOD predictions for flight 5 were calculated using meteorological data from the GMAO. There was only a limited spiral near Four Corners, from 4.5 km to the ground, which was not used for the O_2 analysis. Again, the agreement between theory and experiment as shown in Fig. 10 (right panel) was very good.

Flights 6 and 7 from Palmdale to the midwest (Iowa and Wisconsin) and back provided us with the best opportunity to test the O_2 lidar pressure measurements. The terrain elevation from central Colorado, east of the Rocky Mountains, to the plains of eastern Iowa changes gradually from an altitude of ~1600 m to ~200 m. In the absence of any significant weather system that can change the local meteorological conditions, the change in elevation should produce a corresponding change in DOD and air pressure. Figure 11 shows the DOD comparison and the ground elevation change for the flight segment from Davenport, Iowa to Denver, Colorado for flights 6 and 7. The theoretical DOD was calculated using GMAO data averaged over minutes. The agreement between the O_2 IPDA and the theoretical predictions

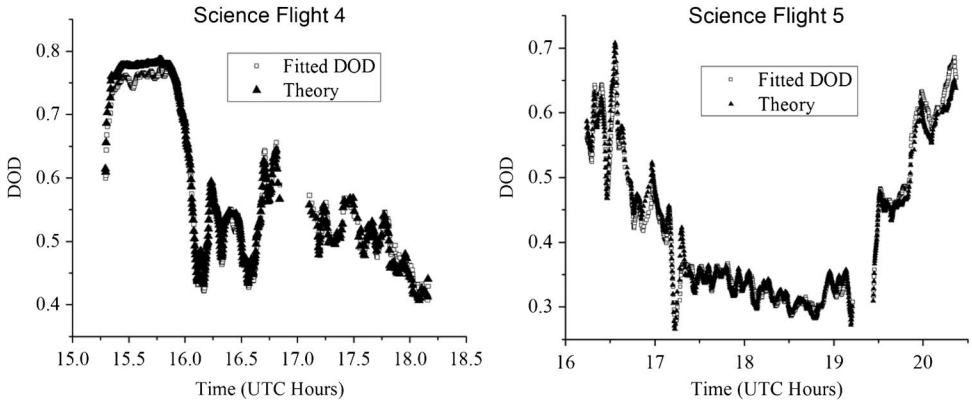

Fig. 10. Experimental and predicted DOD comparison as a function of time for (left) flight 4 and (right) flight 5. Flight 4 shows the transit from California to Oregon and flight 5 shows the entire flight from Palmdale, California, to around the Four Corners power plant in New Mexico. The predicted DOD was calculated using GMAO data with 1 s intervals.

was very good and the lidar tracked the change in elevation (and pressure) as expected.

For these comparisons, we applied the constant scaling factor of 8% obtained in flight 1 to the predicted values of all the other flights. The 8% bias correction is partly due to line mixing and other spectroscopic effects as reported recently by Long *et al.* [23,24], Tran *et al.* [22], and in O_2 GOSAT retrievals [30,31]. In addition, instrumental offsets discussed in more detail in the next section contribute to the bias correction. The remaining random error after the bias correction was 2.5%–3% depending on the signal and background levels.

4. Error Discussion

The high accuracy and precision needed for this measurement pose many challenges for the instrument design. All spectroscopic instruments, regardless of the approach, have systematic and random error sources that limit their accuracy and precision. The theoretical framework for the random error analysis for an IPDA lidar was presented by Abshire *et al.* [13] and Ehret *et al.* [14], and will not be reproduced here. However, systematic instrument bias errors are harder to estimate and their effects depend greatly on the time scale involved. Instrument bias errors such as long-term baseline drifts and etalon fringes are very hard to model effectively but can affect both the accuracy and precision. Furthermore, they vary over time and cannot be reduced by increasing the averaging time or by conventional filtering techniques.

We have addressed several systematic errors in our instrument design: Errors due to cloud and aerosol scattering from thin clouds are minimized by our pulsed approach, which digitizes the entire atmospheric column return and gates the returns from the ground.

Another important consideration is the number of sampling points. IPDA typically uses a minimum of two wavelengths (on- and off-line); however, that simple approach makes the measurement susceptible to systematic errors such as baseline structure and etalon fringes that can bias the retrievals. Our IPDA instrument samples the O_2 line at several points to establish a "zero" transmittance baseline and minimize unwanted etalon effects that can affect the accuracy of the measurement.

The multiwavelength approach, however, has the drawback that each wavelength may experience slightly different reflectivity from the surface. Our pulses are separated by 100 μs. For typical aircraft

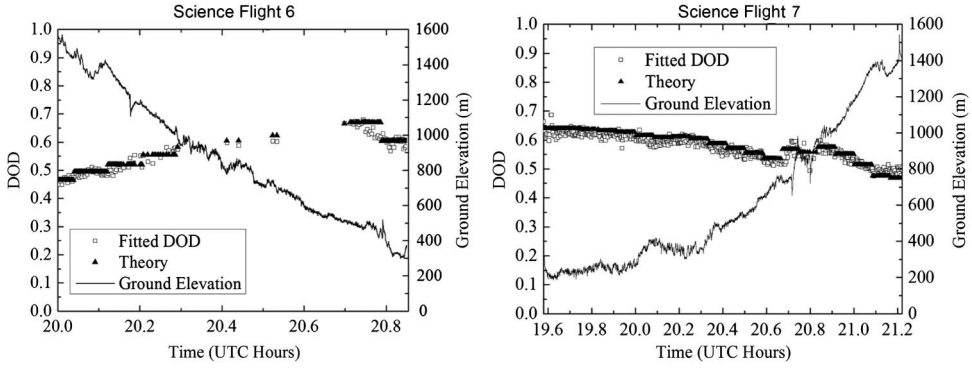

Fig. 11. Experimental and predicted DOD comparison and ground elevation as a function of time for (left) flight 6 and (right) flight 7. The predicted DOD was calculated using GMAO data with 5 min intervals. The flight segments traverse approximately the region between Davenport, Iowa to Denver, Colorado, where the ground elevation changes gradually. The ground elevation was determined by the aircraft radar altimeter and the GPS readings.

speeds of 200 m/s and an altitude of 10 km, subsequent spots on the ground are separated by roughly 2 cm and the spot diameter on the ground is approximately 1.1 m. So there is a significant spot overlap (>98%) between adjacent pulses. If the reflectivity changes radically between the first and last spot (<4 ms or <0.8 m), the effect would be to introduce a slope in the lineshape. Although this is a serious concern, it can be addressed in the retrieval algorithm by introducing a slope in the baseline. In addition, typically a 10 s averaging period is used in the analysis, which effectively averages out most random reflectivity changes.

The total error is, of course, an aggregate of the lidar measurement (transmittance) error, the range error, and the error in estimating the absorption cross section for a given vertical profile of the atmosphere. We can get estimates of these errors from different measurements. Our ground calibrations and earlier airborne measurements from a different aircraft with the CO_2 lidar showed that our absolute range error over flat terrain in 1 s was ~2.8 m [25]. The fractional range error is, of course, a function of altitude but over flat terrain at 10 km we can expect the fractional range error to be small, approximately 0.03%. Over rough terrain, the range error will increase, but overall we do not expect it to exceed 0.1% over 1 s.

The error in the absorption cross section depends on several factors such as the spectroscopic parameters of the oxygen lines (linestrength dependence on temperature, pressure broadening coefficients, line mixing, etc.). These errors have been discussed in some detail by Long and Hodges [24] and Tran *et al.* [22], and can have a significant effect on the retrievals. We selected the particular O_2 lines at 764.7 nm in order to minimize temperature sensitivity. However, the spectroscopic and lineshape parameters for these lines are still being studied and we expect some of the systematic errors due to the spectroscopy to be reduced. The bias correction in O_2 GOSAT retrievals [30,31] are on the order of ~3%. We believe that a portion of our systematic bias error is due to the uncertainty in the current spectroscopic models that we used in the analysis.

Finally, our predicted values ("truth") are affected by our knowledge of the state of the atmosphere. In order to estimate the magnitude of the error due to our incomplete knowledge of the state of the atmosphere, we compared the O_2 OD derived from two sets of meteorological sensors available during flight 1: the aircraft spiral data and data from balloon radiosondes released at the same location during the low-altitude pass over Castle airport. The absolute difference in OD, $OD_{Aircraft} - OD_{Radiosonde}$, and the normalized difference in OD, $(OD_{Aircraft} - OD_{Radiosonde})/OD_{Aircraft}$ at all wavelengths for 12.8 km is shown in Fig. 12. The normalized difference in OD can be as high as 0.4% depending on the wavelength. These estimates, which are based on data obtained from two calibrated sensors at virtually the same location and time, allow us to estimate the error of the absorption cross section error due to our knowledge of the state of the atmosphere.

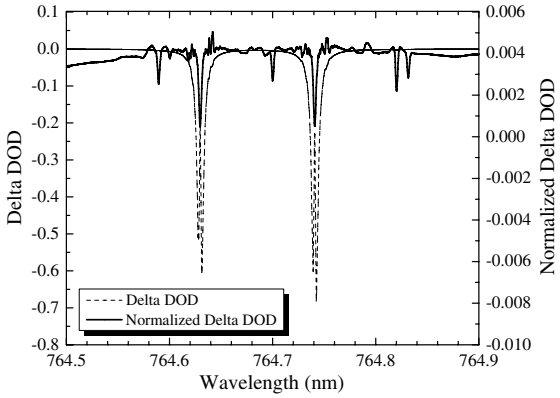

Fig. 12. Theoretical DOD and Normalized DOD comparison at 10 km from airplane and radiosonde data for flight 1.

The estimates for the range error (~0.03%), the spectroscopic error (~3%), and the state of the atmosphere error (~0.4%) are still well below the total 8% bias we observed in our flights. Thus we can conclude that, although they contribute to the overall error, the main contribution to the total error is dominated by the lidar OD measurement error.

We estimate that our random errors are on the order of 2%–3% depending on the signal strength and background counts. Our returns are typically between 100 and 300 counts with a standard deviation of 2–5 counts, resulting in a percentage error of 2%–3%. The random errors can be improved by increasing the laser energy, limiting the background counts by reducing the FOV, improving the dynamic range and performance of the receiver, and increasing the averaging period. We are currently in the process of improving the SNR of our system by using a more powerful amplifier and improving the dynamic range of our receiver. The maximum output energy per pulse of our fiber amplifier at 1529.3 nm was 10–12 μJ which, after doubling, results in ~1.5–2 μJ at 764.7 nm. We have placed an order for a power amplifier that would scale the 1529.3 nm energy up to 60–120 μJ with a corresponding energy increase at 764.7 nm (a factor of 5–10). If the power amplifier meets its specifications, we expect to reduce the random noise component by a factor of $\sqrt{10} \sim 3.3$ from 2%–3% to 0.6%–1%. Increasing the signal energy would also require an increase in the dynamic range of our receiver. We are in the process of implementing an 8-channel receiver to increase the dynamic range of our instrument. Purchasing detectors with lower dark count rate should also help, although the reduction in random error may be relatively small.

However, it is systematic errors and not random errors (such as normalization of the transmitted pulse energy and etalon fringes) that are presently the limiting error sources in our system. The 8% systematic bias we observed is probably due to imperfect normalization of the filter transmission

we used in our receiver, incorrect nonlinear SPCM count correction, imperfect energy monitor, and baseline structure due to etalon fringes. Our bandpass filter is 0.5 nm wide (FWHM) which is roughly the span of our wavelength scan. The narrow filter is necessary in order to limit the solar background counts. The narrow filter spectral response can distort the wings of the received line shape and introduce a systematic offset that cannot be easily discerned. Although we calibrated the transmission of the filter in the laboratory prior to flight, small changes in the incidence angle and temperature may introduce an additional bias. We estimate a 1° change in the incidence angle would produce a 55 pm shift in the transmission peak of the filter. The retrieval algorithm tries to account for a shift in the filter transmission peak by moving the filter pass band. In the future, we plan to implement a more robust optomechanical design and an *in situ* filter preflight calibration to account for any shifts.

The SPCM nonlinearity is also a significant factor, especially in cases where overlapping pulses can cause photon-counting losses [32]. This was particularly problematic in the Pacific Northwest flight, where the reflectivity changed rapidly because of the intermittent snow cover, and some of the other flights where we flew close to bright, highly reflecting clouds. The SPCM dynamic range could not accommodate the rapid change in background signal and it is more difficult to accurately account for the nonlinear effects. In our analysis, we used the correction supplied by the manufacturer but we suspect it may be inadequate, especially in the wings of the absorption, and may account for some of our bias error. We are currently in the process of improving the nonlinear SPCM count correction. In addition, we are improving the dynamic range of the receiver by increasing the laser energy and splitting the signal into multiple SPCMs.

The energy monitor is another source of systematic error. Ideally the monitor should be a perfect representation of the outgoing pulse energy and should be used to normalize the received energy. In practice, that is never the case. Varying detector response, etalon fringes, beam pointing and sampling issues, and other effects combine to degrade the performance of the energy monitor. Although the use of the integrating sphere minimizes some of these issues, there are still improvements to be made, such as temperature control of the detector and the use of separate spheres for CO_2 and O_2. The integrator electronics which monitor the outgoing pulse energy may also introduce a small bias in the measured pulse energies. The bias is calibrated on the ground prior or after the flights. However, it is possible that it may vary during flight as the temperature of the electronics changes. We are currently trying to substitute our integrator electronics with fast digitizers that will sample the pulse waveform to mitigate this issue.

The spectral purity of the transmitter could potentially account for part of the large systematic error in our measurements. The specifications of the seed (diode) DFB laser provided by the manufacturer list the laser linewidth as 1 MHz and the single-mode suppression ratio to be at least 45 dB. We have also measured the fiber amplifier and the doubler output spectral purity using an optical spectrum analyzer. Our results show that there is no significant emission outside the main peak at 764.7 nm, which is about 65 dB above the noise floor (Fig. 13). The resolution of the measurement was 10 pm (5.1 GHz).

Finally, another nonrandom noise component that limited our retrievals was etalon fringes in our instrument. Etalon fringes are unwanted optical interference patterns that arise from multiple weak reflections from each optical surface in the optical path. If they remained fixed they would simply introduce a constant offset to our signal that can, in principle, be subtracted. However, their phase, period, and amplitude are a function of small path length changes due to optomechanical shifts, vibration, temperature and pressure changes, and changes in the index of refraction of various optical elements. As a result, etalon fringes introduce a time-dependent, nonstationary background structure that is often indistinguishable from the signal of interest and cannot be filtered out by conventional noise-filtering techniques. Etalon fringes have been observed in laser spectrometers for a long time and have been shown to limit the precision, accuracy, and averaging time of laser spectrometers [10,33]. Ways to mitigate them and reduce their impact include careful optomechanical design using wedged and AR-coated optics, the use of reflective versus transmissive optics, frequent calibrations using a reference cell with background (null) gas, mechanical or electronic dithering methods [34–36], and various signal-processing techniques [37–41]. Some of these methods, like a reference cell with background gas, are mostly applicable to *in situ* spectrometers but are not easily adaptable to airborne or space atmospheric measurements. Others, like mechanical

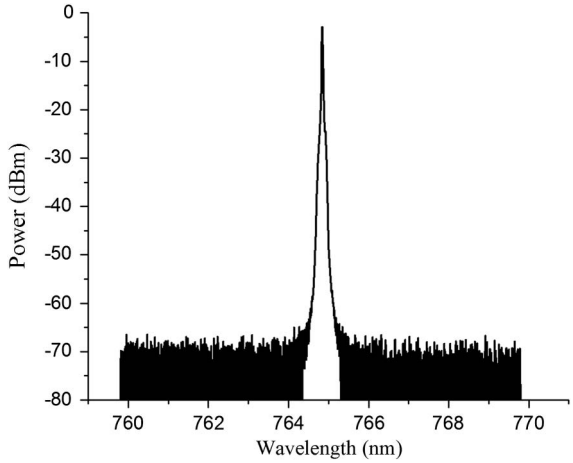

Fig. 13. Laser emission spectrum measurement using an optical spectrum analyzer. The emission peak is at 764.7 nm, which is 65 dB above the noise floor. The resolution of the measurement was 10 pm (5.1 GHz).

dithering, may not be desirable in a space instrument where the use of mechanisms that can fail in orbit is not considered good engineering practice. In our instrument, we have tried to minimize etalon fringes in several ways. We have used special AR-coated and wedged optics. All of our beam splitters/combiners are AR coated and wedged and all of our fibers, filters, and beam expanders are also AR coated. We have also made use of reflective as opposed to transmissive optics whenever possible. For example, we have removed the triplet correction lenses from our commercial telescope and used special AR-coated fibers to achieve the desired FOV. We have also used an integrating sphere with a wedged, AR-coated beam splitter for the energy monitor. But ultimately it is unrealistic to expect that etalon fringes can be completely eliminated in a field instrument with commercial off-the-shelf parts and limited resources. Much remains to be done. We are in the process of redesigning some of the optics in our transmitter and receiver to reduce the number of transmissive optics. We are also talking to the detector manufacturer to see if the detector windows can be AR coated at the factory. We have investigated the use of signal-processing techniques such as matched [38] and Kalman filters [40] and a Singular Value Decomposition Algorithm [39] to reduce the effect of fringes, but the improvement has been minimal. We are exploring additional signal-processing techniques based on neural networks to identify and discriminate nonstationary noise (e.g., a time-varying baseline structure due to etalon fringes) from our trace gas signal. We hope that these efforts will improve our accuracy and precision in the long term.

5. Summary

We have demonstrated initial airborne measurements of atmospheric OD using the Oxygen A-band and a multiwavelength IPDA lidar over varying topography and terrain and up to altitudes of 13 km. The lidar uses a doubled erbium-doped fiber laser with single photon-counting detectors and the Oxygen A-band at 765 nm to measure the column abundance of O_2.

The O_2 IPDA lidar flew seven science flights in the continental United States and British Columbia, Canada in 2011. Our results from five of the flights show good agreement between the experimentally derived DOD measurements with the theoretical predictions for aircraft altitudes from 3 to 13 km after a systematic bias correction of approximately 8% was applied. We estimate that the random noise component is 2.5%–3%. Our errors are above the current estimates of what can be obtained with meteorological data and radiosonde networks in the US. However, the existing recommendation from the ASCENDS working group is still that "co-located surface pressure measurements" are needed for ASCENDS and that "the currently available surface pressure forecasts and/or re-analyses from numerical weather models [are] insufficiently accurate, especially over sparsely observed areas, to relax the need for concurrent measurement of pressure" [3]. The ASCENDS working group will revisit this requirement in the near future. Presently, no official pressure measurement requirement has been released for ASCENDS, but we do anticipate that a measurement error of ~0.2% will be needed in order to keep the $X(CO_2)$ retrieval error below 1 ppm.

We are trying to address both systematic (bias) and random noise errors in our system in order to meet the anticipated ASCEND requirements. Our main random error sources are the low signal levels and the high solar background. We expect that, with our new higher energy amplifier, we will reduce the random noise component by a factor of $\sqrt{10} \sim 3.3$ from 2%–3% to 0.6–1%. Higher energies would be needed to further reduce the random error and we are exploring several power scaling approaches with two different industrial partners. We are also in the process of increasing the dynamic range of our instrument.

Reducing the solar background on the detector should also reduce the random error. There are two ways to reduce the solar background: reduce the bandpass of the receiver or reduce the FOV. The receiver bandpass is already narrow (0.5 nm) and cannot be reduced further without severely distorting the lineshape. The FOV in the current instrument, however, could be reduced from 200 to 150 μrad (or less if the boresight can be held stable). Reducing the FOV to 150 μrad should reduce the solar background and improve our random error by a factor of $(200/150)^2$ or 1.8, bringing the random error closer to the requirement. For a space instrument, the FOV could be reduced further with much better optomechanical design and a boresight adjustment mechanism.

Addressing systematic errors may prove even more challenging. As stated above, we are currently implementing improvements in our laser energy monitor normalization hardware and software, the overall optomechanical design of the transceiver, our wavelength calibration, and the nonlinear receiver correction of our system to reduce these systematic errors. We are also investigating the impact of spectroscopic effects such as line mixing on the O_2 spectra in our retrievals. We anticipate that these improvements will address both systematic (bias) and random noise errors in our system.

For the space instrument, our calculations show that the energy would have to be scaled to ~4 mJ assuming a 1.0 m receiver diameter and a photon-counting detector with a quantum efficiency of 65% and an instrument FOV of 75 μrad. The photon-counting detectors we are proposing to use have a high technology readiness level (TRL) and have flown successfully on NASA's ICESat mission [42]. Large high TRL receiver telescopes have also flown previously on other space lidar missions [42–44], and the European Space Agency Aeolus-ADM Wind Mission [45] has developed a 1.5 m SiC telescope that

is well suited for ASCENDS. Our current airborne lidar uses EDFAs. Scaling the energy to 4 mJ in a single EDFA has so far proven difficult because of nonlinear effects such as stimulated Brillouin scattering. However, multiple EDFA beams could be combined to produce the energy needed for space. Alternatively, an EDFA can serve as a first stage or preamplifier to a power amplifier based on different technologies such as planar waveguide amplifiers [46]. We have carried out studies with several industrial partners using both approaches for space and found no fundamental technical barriers so far. We will continue to develop these technologies in order to meet the ASCENDS requirements.

We would like to acknowledge the support of the NASA Earth Science Technology Office (ESTO) Instrument Incubator Program (IIP), the NASA ASCENDS Program, and the Goddard IRAD program for funding this research. We would also like to express our appreciation to NASA's Dryden Aircraft Operations Facility, in Palmdale, California and the DC-8 flight and ground crews for their support during the flights.

References

1. "Intergovernmental Panel on Climate Change Report (IPCC)," 2007, http://www.ipcc.ch/index.htm.
2. National Research Council Decadal Survey, *Earth Science and Applications from Space: National Imperatives for the Next Decade and Beyond* (National Academic, 2007).
3. "NASA ASCENDS Workshop," http://cce.nasa.gov/ascends/index.htm.
4. C. L. Korb and C. Y. Wang, "Differential absorption lidar technique for measurement of the atmospheric pressure profile," Appl. Opt. **22**, 3759–3770 (1983).
5. K. J. Ritter, "A high resolution spectroscopic study of absorption line profiles in the A-Band of molecular oxygen," Ph.D. dissertation (University of Maryland, 1986).
6. G. K. Schwemmer, M. Dombrowski, C. L. Korb, J. Milrod, H. Walden, and R. H. Kagann, "A lidar system for measuring atmospheric pressure and temperature profiles," Rev. Sci. Instrum. **58**, 2226–2237 (1987).
7. C. N. Flamant, G. K. Schwemmer, C. L. Korb, K. D. Evans, and S. P. Palm, "Pressure measurements using and airborne differential absorption lidar. Part I: analysis of the systematic error sources," J. Atmos. Ocean. Technol. **16**, 561–574 (1999).
8. M. Stephen, M. Krainak, H. Riris, and G. R. Allan, "Narrowband, tunable, frequency-doubled, erbium doped fiber-amplified transmitter," Opt. Lett. **32**, 2073–2075 (2007).
9. X. Sun and J. Abshire, "Comparison of IPDA lidar receiver sensitivity for coherent detection and for direct detection using sine-wave and pulsed modulation," Opt. Express **20**, 21291–21304 (2012).
10. P. Werle, "Accuracy and precision of laser spectrometers for trace gas sensing in the presence of optical fringes and atmospheric turbulence," Appl. Phys. B **102**, 313–329 (2011).
11. L. S. Rothman, I. E. Gordon, A. Barbe, D. Chris Benner, P. F. Bernath, M. Birk, V. Boudon, L. R. Brown, A. Campargue, J. P. Champion, K. Chance, L. H. Coudert, V. Dana, V. M. Devi, S. Fally, J.-M. Flaud, R. R. Gamache, A. Goldman, D. Jacquemart, I. Kleiner, N. Lacome, W. J. Lafferty, J. Y. Mandin, S. T. Massie, S. N. Mikhailenko, C. E. Miller, N. Moazzen-Ahmadi, O. V. Naumenko, A. V. Nikitin, J. Orphal, V. I. Perevalov, A. Perrin, A. Predoi-Cross, C. P. Rinsland, M. Rotger, M. Šimečková, M. A. H. Smith, K. Sung, S. A. Tashkun, J. Tennyson, R. A. Toth, A. C. Vandaele, and J. Vander Auwera, "The HITRAN 2008 molecular spectroscopic database," J. Quant. Spectrosc. Radiat. Transfer **110**, 533–572 (2009).
12. R. Measures, *Laser Remote Sensing* (Wiley, 1984).
13. J. B. Abshire, H. Riris, G. Allan, C. J. Weaver, J. Mao, X. X. Sun, W. E. Hasselbrack, R. S. Kawa, and S. Biraud, "Pulsed airborne lidar measurements of atmospheric CO_2 column absorption," Tellus **62B**, 770–783 (2010).
14. G. Ehret, C. Kiemel, W. Wirth, A. Amediek, A. Fix, and S. Houweling, "Space-borne remote sensing of CO_2, CH_4, and N_2O by integrated path differential absorption lidar: a sensitivity analysis," Appl. Phys. B **90**, 593–608 (2008).
15. W. B. Grant, "Effect of differential spectral reflectance on DIAL measurements using topographic targets," Appl. Opt. **21**, 2390–2394 (1982).
16. C. Kiemle, M. Quatrevalet, G. Ehret, A. Amediek, A. Fix, and M. Wirth, "Sensitivity studies for a space-based methane lidar mission," Atmos. Meas. Tech. Discuss. **4**, 3545–3592 (2011).
17. J. R. Chen, K. Numata, and S. T. Wu, "Error reduction methods for integrated-path differential-absorption lidar measurements," Opt. Express **20**, 15589–15609 (2012).
18. J. B. Abshire, H. Riris, C. J. Weaver, J. Mao, G. R. Allan, W. E. Hasselbrack, and E. V. Browel, "Airborne measurements of CO_2 column absorption and range using a pulsed direct detection IPDA lidar," Appl. Opt. **52**, 4446–4461 (2013).
19. J. Humlicek, "Optimized computation of the Voigt and complex probability functions," J. Quant. Spectrosc. Radiat. Transfer **27**, 437–444 (1982).
20. J. Liu, J. Lin, G. Huang, Y. Guo, and C. Duan, "Simple empirical analytical approximation to the Voigt profile," J. Opt. Soc. Am. B **18**, 666–672 (2001).
21. R. H. Dicke, "The effect of collisions upon the Doppler width of spectral lines," Phys. Rev. **89**, 472–473 (1953).
22. H. Tran, C. Boulet, and J. M. Hartmann, "Line mixing and collision-induced absorption by oxygen in the A band: laboratory measurements, model, and tools for atmospheric spectra computations," J. Geophys. Res. **111**, D15210 (2006).
23. D. A. Long, D. K. Havey, M. Okumura, C. E. Miller, and J. T. Hodges, "O_2 A-band line parameters to support atmospheric remote sensing," J. Quant. Spectrosc. Radiat. Transfer **111**, 2021–2036 (2010).
24. D. A. Long and J. T. Hodges, "On spectroscopic models of the O_2 A-band and their impact upon atmospheric retrievals," J. Geophys. Res. **117**, D12309 (2012).
25. A. Amediek, X. Sun, and J. B. Abshire, "Analysis of range measurements from a pulsed airborne CO_2 integrated path differential absorption lidar," IEEE Trans. Geosci. Remote Sens. **51**, 2498–2504 (2013).
26. C. Rodgers, *Inverse Methods for Atmospheric Soundings, Theory and Practice*, Vol. **2** of Series on Atmospheric, Oceanic and Planetary Physics (World Scientific, 2000).
27. S. R. Kawa, J. Mao, J. B. Abshire, G. J. Collatz, X. Sun, and C. J. Weaver, "Simulation studies for a space-based CO_2 lidar mission," Tellus **62B**, 759–769 (2010).
28. S. A. Clough and M. J. Iacono, "Line-by-line calculations of atmospheric fluxes and cooling rates. 2: applications to carbon dioxide, ozone, methane, nitrous oxide, and the halocarbons," J. Geophys. Res. **100**, 16519–16535 (1995).
29. "Goddard Modeling and Assimilation Office," http://gmao.gsfc.nasa.gov/.
30. A. Butz, S. Guerlet, O. Hasekamp, D. Schepers, A. Galli, I. Aben, C. Frankenberg, J.-M. Hartmann, H. Tran, A. Kuze, G. Keppel-Aleks, G. Toon, D. Wunch, P. Wennberg, N. Deutscher, D. Griffith, R. Macatangay, J. Messerschmidt, J. Notholt, and T. Warneke, "Toward accurate CO_2 and CH_4 observations from GOSAT," Geophys. Res. Lett. **38**, L14812 (2011).
31. D. Crisp, B. M. Fisher, C. O'Dell, C. Frankenberg, R. Basilio, H. Bösch, L. R. Brown, R. Castano, B. Connor, N. M. Deutscher, A. Eldering, D. Griffith, M. Gunson, A. Kuze, L. Mandrake, J. McDuffie, J. Messerschmidt, C. E. Miller, I. Morino, V. Natraj, J. Notholt, D. M. O'Brien, F. Oyafuso, I. Polonsky, J. Robinson, R. Salawitch, V. Sherlock, M. Smyth, H. Suto, T. E. Taylor, D. R. Thompson, P. O. Wennberg, D. Wunch, and Y. L. Yung, "The ACOS CO_2 retrieval algorithm—Part II: global XCO_2 data characterization," Atmos. Meas. Tech. **5**, 687–707 (2012).

32. D. P. Donovan, J. A. Whiteway, and A. I. Carswell, "Correction for nonlinear photon-counting effects in lidar systems," Appl. Opt. **32**, 6742–6753 (1993).
33. P. Werle, R. Mucke, and F. Slemr, "The limits of signal averaging in atmospheric trace-gas monitoring by tunable diode-laser absorption spectroscopy (TDLAS)," Appl. Phys. B **57**, 131–139 (1993).
34. C. R. Webster, "Brewster-plate spoiler: a novel method for reducing the amplitude of interference fringes that limit tunable-laser absorption sensitivities," J. Opt. Soc. Am. B **2**, 1464–1470 (1985).
35. J. A. Silver, D. S. Bomse, and A. C. Stanton, "Diode laser measurements of trace concentrations of ammonia in an entrained-flow coal reactor," Appl. Opt. **30**, 1505–1511 (1991).
36. D. T. Cassidy and J. Reid, "Harmonic detection with tunable diode lasers-two-tone modulation," Appl. Phys. B **29**, 279–285 (1982).
37. P. Werle, P. Mazzinghi, F. D'Amato, M. De Rosa, K. Maurer, and F. Slemr, "Signal processing and calibration procedures for in situ diode-laser absorption spectroscopy," Spectrochim. Acta Part A **60**, 1685–1705 (2004).
38. H. Riris, C. B. Carlisle, R. E. Warren, and D. E. Cooper, "Signal to noise ratio enhancement in frequency modulation spectrometers using digital signal processing," Opt. Lett. **19**, 144–146 (1994).
39. D. S. Bomse and D. J. Kane, "An adaptive singular value decomposition (SVD) algorithm for analysis of wavelength modulation spectra," Appl. Phys. B **85**, 461–466 (2006).
40. H. Riris, C. B. Carlisle, and R. E. Warren, "Kalman filtering of tunable diode laser spectrometer absorbance measurements," Appl. Opt. **33**, 5506–5508 (1994).
41. D. P. Leleux, R. Claps, W. Chen, F. K. Tittel, and T. L. Harman, "Applications of Kalman filtering to real-time trace gas concentration measurements," Appl. Phys. B **74**, 85–93 (2002).
42. J. B. Abshire, X. Sun, H. Riris, J. M. Sirota, J. F. McGarry, S. Palm, D. Yi, and P. Liiva, "Geoscience laser altimeter system (GLAS) on the ICESat mission: on-orbit measurement performance," Geophys. Res. Lett. **32**, L21S02 (2005).
43. A. W. Yu, S. X. Li, M. A. Stephen, A. J. Martino, J. R. Chen, M. A. Krainak, S. Wu, H. Riris, J. B. Abshire, D. J. Harding, G. R. Allan, and K. Numata, "Spaceborne laser transmitters for remote sensing applications," Proc. SPIE **7808**, 780817 (2010).
44. W. H. Hunt, D. M. Winker, M. A. Vaughan, K. A. Powell, P. L. Lucker, and C. Weimer, "CALIPSO lidar description and performance assessment," J. Atmos. Ocean. Technol. **26**, 1214–1228 (2009).
45. O. Reitebuch, "The spaceborne wind lidar mission ADM-Aeolus," in *Atmospheric Physics, Research Topics in Aerospace* (Springer-Verlag, 2012), pp. 815–827.
46. A. W. Yu, M. A. Krainak, D. J. Harding, J. B. Abshire, and X. Sun, "Topographic mapping from space," Proc. SPIE **7467**, 746702 (2009).